Double-*K*-shell ionization of Mg and Si induced in collisions with C and Ne ions

M. Kobal, M. Kavčič, and M. Budnar
J. Stefan Institute, P.O. Box 3000, SI-1001 Ljubljana, Slovenia

J.-Cl. Dousse, Y.-P. Maillard, O. Mauron, and P.-A. Raboud
Physics Department, University of Fribourg, CH-1700 Fribourg, Switzerland

K. Tökési
Institute of Nuclear Research of the Hungarian Academy of Sciences (ATOMKI), P.O. Box 51, H-4001 Debrecen, Hungary
(Received 9 July 2004; published 28 December 2004)

The satellite and hypersatellite *K* x-ray emission of a thin Mg foil and thick polycrystalline Si target bombarded by 34-MeV C and 50-MeV Ne ions was measured using high-resolution crystal diffractometry. The corresponding projectile reduced velocities v/v_K were 1.09 and 0.92 for C ions and 1.02, 0.86 for Ne ions in case of Mg and Si targets, respectively. An energy resolution of approximately 0.5 eV enabled separation of contributions corresponding to states with different numbers of *K*- and *L*-shell vacancies. The relative intensities of satellite and hypersatellite lines were determined by fitting the measured spectra with line shapes calculated using the GRASP92 computer code. To determine the production yields of initial states from the measured x-ray yields, the total decay schemes of initial states were considered. The decay schemes were also used to determine the relative intensities of components contributing to the observed $K\alpha$ satellites and hypersatellites and $K\beta$ satellite intensities. Including theoretical predictions in the fitted model is crucial to analyze properly the $K\alpha$ hypersatellite region which overlaps the $K\beta$ satellites. The initial-state production yields were then used to determine the *L*-shell ionization probabilities and the double- to single-*K*-shell ionization ratio corresponding to the four investigated collisions. The experimental values were compared to the theoretical predictions obtained within the independent electron model using single-electron ionization probabilities calculated by the three-body classical trajectory Monte Carlo (CTMC) method. Since the targets used were thick enough, the equilibrium projectile charge-state distributions in the solid media were assumed. While for the double- to single-*K*-shell ionization ratios a satisfactory agreement was observed between the CTMC predictions and our experimental results, the *L*-shell ionization probabilities were found to be overestimated by the CTMC calculations by a factor of about 2.

DOI: 10.1103/PhysRevA.70.062720 PACS number(s): 32.80.Hd, 32.30.Rj, 32.70.Fw

I. INTRODUCTION

Because of reduced nuclear charge screening due to additional vacancies in the inner shells, x-ray lines emitted by multiply ionized atoms are shifted towards higher energies as compared to diagram lines of singly ionized atoms. In general, the energy shift increases with the principal quantum number of the electron undergoing the transition and is most pronounced in the case of an additional vacancy in the *K* shell. Spectral contributions corresponding to doubly *K* ionized atoms are called *K* hypersatellites, while contributions corresponding to additional vacancies in the *L* shell are called *L* satellites. Apart from $K\alpha$ transitions, where the active electrons are from the $2p$ subshell, there are also $K\beta$ transitions involving $3p$-subshell electrons, but the latter are in the case of Mg and Si almost two orders of magnitude less probable. By measuring the x-ray spectra and identifying different contributions, one can infer on the number of vacancy states produced in collisions. In the case of light elements such as Mg and Si there is an overlap of different contributions and also each separate contribution cannot be described by a single peak. While this rich structure gives us the opportunity to study radiation properties of the target atoms, it also makes proper peak identification and spectra analysis more difficult.

Several experiments with heavy ions on low-*Z* elements have been performed in the past [1–3]. Hypersatellites have been resolved in these works, but due to the high probability of additional ionization in outer shells, resulting in complex x-ray spectra, hypersatellite intensities could not be determined accurately. In experiments with protons, however, where additional outer shell ionization is less probable, double-ionization cross sections for some low-*Z* elements could be obtained [4]. The same is true for heavy ions on mid-*Z* atoms [5], where additional outer-shell ionization was also negligible. In both cases the dominant ionization mechanism was direct Coulomb ionization, since the collisions were quite asymmetric ($Z_{\text{projectile}} \ll Z_{\text{target}}$).

In the case of more symmetric collisions, capture of inner-shell electrons into the empty shells of the projectile becomes important and in some cases even prevails. A detailed investigation of the relative importance of the two main ionization mechanisms has been made for Ti bombarded by heavy ions by Hall *et al.* [6,7]. A similar experimental procedure has also been used by Tribedi *et al.* [8] to obtain double-*K*-shell ionization and electron transfer cross sections for Fe and Ni targets.

Since the majority of experiments have been performed with semiconductor detectors, contributions corresponding to states with different numbers of *L*-shell vacancies could not

be resolved and therefore different fluorescence yields for these contributions were not considered. In the case of Mg and Si where the $K\alpha$ hypersatellites and $K\beta$ satellites are overlapping, the use of a high-resolution instrument is mandatory. However, even instrumental broadening as small as 0.5 eV is not sufficient alone to unravel completely the complex spectra and a detailed theoretical modeling of the target x-ray emission is needed. As a consequence of these difficulties, which are very difficult to overcome, quantitative experimental data for double-*K*-shell ionization of light *Z* elements such as Mg and Si induced in collisions with heavy ions are very scarce.

In this work we report on high-resolution measurements of the $K\alpha$ spectra of Mg and Si induced by collisions with 34-MeV C and 50-MeV Ne ions. The main goal of the project was to determine the double- to single-*K*-shell ionization ratios for the four investigated collisions. The projectile energies were chosen to maximize *K*-shell ionization. As the *L*-shell ionization probabilities are also quite high at these energies, rich satellite structures corresponding to states with up to five additional *L*-shell vacancies were observed. To obtain a credible model of the measured spectra, the line shapes of spectral contributions were calculated by the GRASP92 computer code, and the number of free parameters in the fit was reduced by calculating the decay schemes of initial states. The decay schemes were also used to determine the state production yields from the measured photon yields. As the investigated collisions are nearly symmetric, the probabilities for electron capture and direct ionization are expected to have the same magnitude. Both processes were thus considered in the calculations. The ionization probabilities were calculated within the independent electron approximation, using single-electron ionization probabilities calculated within the three-body classical trajectory Monte Carlo method. Obtained results were compared to the experimental values.

II. EXPERIMENT

The experiment was performed at the variable-energy cyclotron of the Paul Scherrer Institute in Villigen, Switzerland. Metallic foil of Mg (0.35 mg cm^{-2}) and a thick polycrystalline Si target (0.23 g cm^{-2}) were bombarded by 34-MeV C^{2+} and 50-MeV Ne^{3+} ions. Beam intensities of 10–100 nA were used. The spectra were measured with a high-resolution von Hamos Bragg type crystal spectrometer which was described in detail in [9]. The basic elements of the spectrometer are the target-slit system which defines the x-ray source viewed by the crystal, a cylindrically bent crystal, and a position-sensitive x-ray detector. For a given crystal-detector position the energy window of collected x rays is limited by the detector length. To cover different energy regions the crystal and detector are translated along their axes in a way that the slit-to-crystal and crystal-to-detector distances are kept equal. The whole spectrometer is enclosed in a $180 \times 62 \times 24.5$ cm^3 stainless steel vacuum chamber evacuated by a turbo molecular pump down to 10^{-5} Pa. For the Mg measurements performed in second order of reflection the spectrometer was equipped with a T*l*AP(001) crystal ($2d = 25.778$ Å), whereas for Si first-order reflection on the SiO_2 $(1\bar{1}0)$ crystal ($2d = 8.5096$ Å) was used. The crystals were 5 cm wide and 10 cm high with a curvature radius of 25.4 cm. Reflected photons were detected by a 27.65 mm long and 6.9 mm high Peltier cooled CCD (charged coupled device) detector with a pixel size of 27×27 μm^2 and a depletion depth of 50 μm. The detector was thermoelectrically cooled to −60 °C. The background was reduced by sorting good event pixels with selected energy windows. For energy calibration, photoinduced $K\alpha$ x-ray spectra of Mg, Al, Si, and P were employed, using the bremsstrahlung from an x-ray tube with a Cr anode for the production of the target fluorescence.

As the slit is positioned between the target and the crystal, different parts of the detector collect x rays emitted from different parts of the target. The beam intensity distribution on the target is therefore directly reflected in the measured spectra. Although it is possible to correct the spectra by measuring the beam intensity profile, errors are introduced as a result of the beam position fluctuations. Usually defocused beams are used and the errors are insignificant. In this project, however, focused beams had to be used in order to obtain a sufficient signal-to-noise ratio, and the instability of the beam position represented by far the largest source of uncertainty.

The beam intensity profile on the target was determined by measuring $K\alpha$ intensities at different target positions along the direction of the incoming beam. So collected $K\alpha$ yields are directly proportional to the beam intensity profile across the target. The measured beam intensity profiles were then used to correct offline the measured spectral intensities. The experimental errors of the profile corrections were estimated at 5% and an additional error of 10% was considered to account for the finite stability of the beam position.

Since at fixed crystal-detector position the energy interval covered by the spectrometer was around 40 eV, the measurement of each spectrum was performed by collecting data at seven different crystal-detector positions, with an overlap of 100 pixels between the neighboring parts. The spectra collected at different positions were normalized offline to account for the nonhomogeneous beam intensity profile on the target and different exposure time. Since only the signal is affected by the beam intensity profile, at least background of one partial spectrum is needed to normalize two neighboring spectra. The background is easily obtained in the region before the $K\alpha$ diagram line were no signal is expected, so we started normalization at the low-energy part. The intensity of the second partial spectrum was normalized to the first one by multiplying it by a correction factor so that the same intensity was obtained in the overlap region, both spectra been corrected before hand for the beam intensity profile and different levels of background. The same method was employed to adjust the intensities of the third partial spectrum and so on. This way of data normalization resulted in larger uncertainties in the higher-energy regions of the spectra. The overall experimental error in intensities of the final seventh part of the total measured spectrum ranged from 20% to 30%. It should be noted that relatively large normalization errors are due to finite stability of the beam.

The normalized spectra were then corrected for detector efficiency, crystal reflectivity, and change in the solid angle and in the target area seen by a single CCD pixel. The efficiency of the CCD detector was governed by absorption in the 0.6 (1 ± 0.05) μm thick SiO_2 dead layer. The crystal reflectivity correction was calculated, using the ideal mosaic crystal picture with correction for crystal absorption [10]. The last two corrections were computed from pure geometrical considerations. In the case of Mg, the largest corrections are due to the change in the solid angle (20%) and crystal reflectivity (10%). For Si, there are two additional abrupt drops above the *K* absorption edge: one in crystal reflectivity (factor of 5) and the other in detector efficiency (30%).

III. DATA ANALYSIS

In order to determine production yields of states with different numbers of vacancies in *K* and *L* shells, the corresponding contributions in the measured spectra must be identified—namely, the $K\alpha$ satellites and hypersatellites. Photon yields must then be related to state production yields with the use of decay schemes.

The *L*-shell vacancies can be distributed differently between the 2*s* and 2*p* subshells. Thus, there are atoms with $2s^2 2p^{N-2}$, $2s^1 2p^{N-1}$, and $2s^0 2p^N$ vacancy configurations contributing to a satellite or hypersatellite of order *N*. We will denote them as $L^N a$, $L^N b$, and $L^N c$. Since the line shapes and decay schemes of these three configurations differ substantially, we will treat them separately.

To illustrate the identification problem, refer to Fig. 3. Peak identification below the *K* absorption edge (1303 eV) is relatively simple. There are $K\alpha$ satellites following the $K\alpha$ diagram line in steps of approximately 10 eV. Above the absorption edge there is an overlap of $K\alpha$ hypersatellites and $K\beta$ satellites and proper identification in this region is possible only on the basis of a theoretical model incorporating calculated line shapes and predictions of their positions and relative intensities.

A. Calculation of the line shapes

Radiative transitions are denoted by the initial and final electron configurations. Due to multiplet splitting, there are a number of possible radiative transitions between specific initial and final electron configurations. In light elements the differences in transition energies are larger than the natural linewidths, resulting in complex line shapes. The line shape of a specific transition *T* can be written as

$$T(E,E^C,w)=\left[\sum_i \Gamma_i\right]^{-1}\sum_i \Gamma_i L(E-E_i-E^C,w), \qquad (1)$$

where E_i is the energy of the *i*th transition and Γ_i its intensity. The sum goes over all allowed radiative transitions between initial and final states. Since the natural line shape of a single transition and the spectrometer response are both Lorentzian, a single transition was modeled by a Lorentzian (*L*) with width *w*. The first factor in Eq. (1) ensures normalization of line shapes to 1. The parameter E^C is used to shift the transition lines while keeping their shape fixed. This is useful since the structure of a line shape can be calculated much more accurately than its absolute position. The values of *w* were estimated as the sum of detector resolution and the widths of final and initial states. The state widths of singly ionized atoms were taken from [11]. In the case of atoms with single vacancies in different shells, the Mossé [12] approximation was used. For multiply ionized shells, the values were altered according to the Larkins rule [13], using transition rates of singly ionized atoms [14].

To calculate E_i and Γ_i, the GRASP92 [15] computer code was used. The number of transitions and the corresponding Γ_i were calculated considering only initial and final electron configurations and using the same radial functions for initial and final states. The energies of initial and final states were calculated separately in a multiconfiguration approach. Different additional configurations were considered and the line shapes were tested on the $K\alpha$ satellite part of the measured spectra where separate contributions are clearly visible. The best results for $K\alpha$ spectral contributions were obtained by adding configurations obtained from the original ones by substitutions $3s^2 \rightarrow 3p^2$ and $2s^2 \leftrightarrow 2p^2$.

For Mg the measured $K\alpha$ spectra could be well reproduced by the calculated line shapes, the differences in peak intensities being smaller than 5%, while the peak positions agree within 0.2 eV. Since the calculated $K\beta$ line shapes were found to poorly reproduce the first two $K\beta$ satellites, which are clearly visible in the Mg spectra, one Lorentzian and one Gaussian peak were used to describe single $K\beta$ satellites. In the case of Si, it was not possible to adequately reproduce either the $K\alpha$ or $K\beta$ contributions. By comparing the satellite parts of Mg and Si, it was observed that the line shapes are similar in both cases. Due to a larger nucleus charge, the $K\alpha$ satellites of Si lie at approximately 40% larger energies than the Mg $K\alpha$ satellites and also energy separations between the individual peaks of a specific $K\alpha$ satellite are approximately 40% larger in Si spectra than in Mg spectra. Since Si $K\alpha$ line shapes can be inferred on by knowing the Mg ones, the Si spectra were modeled with pseudo-Voigt curves, using several curves when such a need was observed in the Mg spectra.

B. Decay schemes

In order to relate measured photon yields ($K^X \alpha L^N i$) to the initial vacancy-state yields produced in collisions, decay schemes of initial states $K^X L^N i$ having *X* holes in the *K* shell and *N* holes in the *L* shell were calculated. KL_1L_1, $KL_1L_{2,3}$, $KL_{2,3}L_{2,3}$, KL_1M_1, $KL_1M_{2,3}$, $KL_{2,3}M_1$, $KL_{2,3}M_{2,3}$, $L_1L_{2,3}M_1$, $L_1M_1M_1$, $L_1M_1M_{2,3}$, $L_{2,3}M_1M_1$, $L_{2,3}M_1M_{2,3}$, and $L_{2,3}M_{2,3}M_{2,3}$ Auger transitions, $L_1L_{2,3}M_{2,3}$ Coster-Kronig transitions, and $K\alpha$ ($KL_{2,3}$) and $K\beta$ ($KM_{2,3}$) radiative transitions were considered. The probabilities for all other transitions are less than 10^{-4} and were neglected. Since we did not distinguish between $p_{1/2}$ and $p_{3/2}$ subshells, the subscript 2,3 was used for either of the two. The probabilities for nonradiative transition rates of singly ionized atoms were taken from Perkins *et al.* [14]. In the case of multiply ionized atoms, the values were corrected according to the statistical approach first proposed by Larkins [13]. The $K\alpha$ and $K\beta$

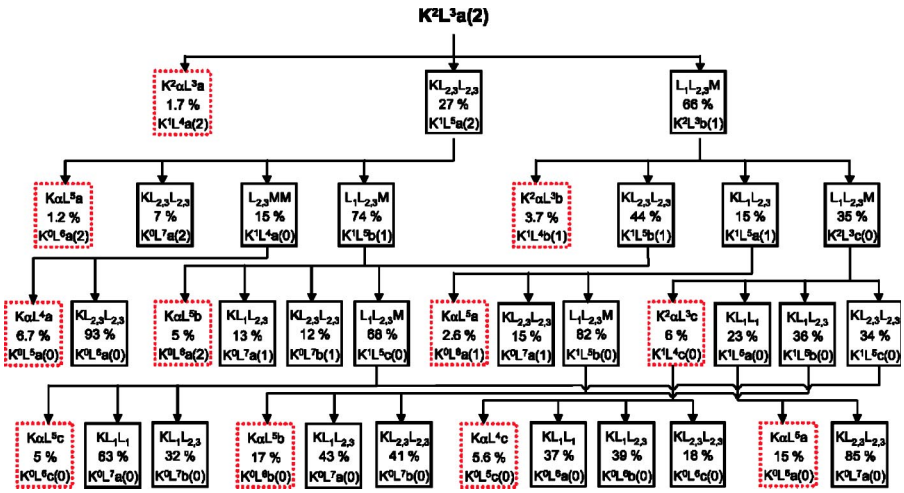

FIG. 1. Decay scheme of the Mg K^2L^3a state with two M-shell electrons. Only transitions with probabilities greater than 5% were considered. The notation in the boxes describes transitions (first lines), their probabilities (second lines), and atomic states after the transition with the number of M-shell electrons shown in parentheses (third lines). The $K\alpha$ transitions (dotted boxes) are included, regardless of their probability. The first line in these boxes describes the emitted photon.

transition rates were derived from K-shell fluorescence yields [16] by applying the Larkins approach.

As an example, the decay scheme of Mg K^2L^3a state is presented schematically in Fig. 1. In the scheme only transitions with probabilities greater than 5% were considered. Since we are interested in photon yields, $K\alpha$ transitions are also shown, regardless of their probability. Figure 1 demonstrates that atomic states K^2L^3a contribute not only to the $K^2\alpha L^3a$ hypersatellite yield, but also to $K^2\alpha L^3b$, $K^2\alpha L^3c$, $K\alpha L^5a$, $K\alpha L^5b$, $K\alpha L^5c$, $K\alpha L^4a$, and $K\alpha L^4c$ photon yields.

Using the decay schemes of all excited states, the relation between the measured photon yields and the initial vacancy-state production yields can be expressed in the following matrix form:

$$Y^\alpha = W^\alpha I. \tag{2}$$

The vector Y^α stands for the $K^X\alpha L^N i$ photon yields and the vector I for the yields of initially produced K^XL^Ni vacancy states. We considered states with one and two K-shell vacancies and up to five L-shell vacancies. In addition there are three possibilities of distributing the L-shell vacancies among the $2s$ and $2p$ subshells ($i=a,b,c$). We were therefore dealing with 36 states, which is also the dimension of Eq. (2). The component indices were assigned according to the values of X, N and i—namely, $18(X-1)+3N+i$.

The same procedure can be followed for $K\beta$ transitions and build W^β matrix from $K\beta$ photon yields. It should be noted that the same states contribute to $K\alpha$ and $K\beta$ transitions, meaning that $K\beta$ photon yields can be determined from $K\alpha$ photon yields and vice versa. Since the same conclusions apply to W^α and W^β we shall use symbol W for both of them.

Decay schemes depend also on the number of M-shell electrons in the initial configuration. Since it is not possible to resolve contributions corresponding to initial states with different numbers of M-shell electrons, the W matrix must be written as a superposition:

$$W = \sum_i P_M(n_M) W(n_M), \tag{3}$$

where n_M is the number of M-shell electrons in the initial state, P_M the probability of producing such a state, and $W(n_M)$ the corresponding decay scheme matrix. It is therefore not possible to relate the photon yields to the initial state production yields without the knowledge of M-shell ionization. The values of P_M were determined using the three-body classical trajectory Monte Carlo simulation as explained in Sec. IV.

Whereas separate $K^X\alpha L^N$ contributions can be clearly resolved in the measured spectra (Figs. 3 and 4), it is not possible to resolve the three components $K^X\alpha L^N i(i=a,b,c)$ within each contribution. However, the initial state yields of the three components can be related to their net K^XL^N initial-state yield by assuming equal ionization probabilities for the $2s$ and $2p$ subshells. Using this assumption, Eq. (2) can be rewritten in a reduced base I_r, and Y_r which now incorporates $I(K^XL^N)$ and $Y(K^XL^N)$:

$$Y_r = W_{rr} I_r. \tag{4}$$

The W matrix in the reduced 16 dimensional base was denoted by W_{rr}. W_{rr} is an upper diagonal matrix and enables direct determination of initial-state yields from the measured photon yields.

In the K x-ray emission of solid Mg targets, spectral lines corresponding to $K\beta$ transitions can be clearly observed even though such transitions are not possible for the free Mg atom, since it has no $3p$ electrons. This can be explained by noting that in the solid Mg target, M-shell electrons belong to the conduction band and have therefore no fixed angular momentum, allowing them to participate also in $K\beta$ transitions. Since M-shell electrons move freely in metal, even if an M-shell electron is ejected from the atom, other electrons rearrange so that the number of M-shell electrons of an atom remains practically the same. To accommodate for these solid state differences, we have considered the M-shell electrons to have $3p$ and $3s$ character and kept the number of M-shell electrons constant during the entire Mg decay schemes.

When measurements are performed on solid targets, stopping of projectiles in the target and absorption of x rays on their way out need to be considered in order to express the measured $K\alpha$ satellite and hypersatellite yields with the ionization cross sections at the projectile impact energy. The

effect of self-absorption can be included by additional matrix F_T in Eq. (4):

$$Y_i \propto \sum_{j \geq i} W_{rr}(i,j) F_T(i,j) \sigma_j(E_0), \tag{5}$$

where σ_j is the cross section for producing a state with index j and E_0 is the projectile impact energy. In case of thin Mg foil the stopping of the projectiles can be neglected and only the absorption coefficients are needed to calculate F_T. In case of Si the projectiles are completely stopped within the thick target. Due to large absorption of photons with energies above the K absorption edge, only the upper 5 μm of the target in which the projectiles lose approximately 10% of their energy contributes to the hypersatellite yield. Since absorption of photons with energies below the K absorption edge is much smaller, the contributions to satellite yields come practically along the entire projectile path (approximately 25 μm). In this case the cross-section energy dependence along the projectile path within the target is also incorporated in the calculation of the F_T matrix. Details of this self-absorption correction are presented in the Appendix.

C. Reducing the number of parameters varied in the fitted model

Due to complex structure of Mg and Si high-resolution spectra induced in heavy-ion collisions, it is important to reduce the number of parameters varied in the fitted model to make it credible. In this section we will calculate the relative intensities of components contributing to each $K\alpha$ satellite and hypersatellite and $K\beta$ satellite yields.

Each spectral contribution $K^X\alpha L^N$ is generally composed of three components $K^X\alpha L^N i$ $(i=a,b,c)$ corresponding to different distribution of L-shell vacancies between the $2s$ and $2p$ subshells. Knowing the relative intensity ratios and the line shapes of these three components, the line shapes of spectral contributions $K^X\alpha L^N$ are well determined. This allows the calculated line shapes to be tested on the measured spectra and also helps peak identification in the $K\alpha$ hypersatellite region.

The relative intensities of components $K^X\alpha L^N i$ contributing to a given $K^X\alpha L^N$ contribution are defined as

$$\eta(K^X\alpha L^N i) = \frac{Y(K^X\alpha L^N i)}{Y(K^X\alpha L^N a) + Y(K^X\alpha L^N b) + Y(K^X\alpha L^N c)}. \tag{6}$$

The values of η can be determined from the W^α matrix in the following way. From the experimentally measured $Y(K^X\alpha L^N)$, $I(K^X L^N)$ can be obtained using Eq. (4). Assuming equal ionization probabilities for the $2s$ and $2p$ subshells, the values of $I(K^X L^N)$ can be related to the values of $I(K^X L^N i)$, which are in turn related to $Y(K^X\alpha L^N i)$ by Eq. (2). The latter can then be used in Eq. (6) to finally obtain the values of η. Since these values are used in the fitting procedure to determine $Y(K^X\alpha L^N)$ yields, an iterative approach is needed.

In the first step of the iterative procedure one can assume that only $K^X L^N$ states contribute to the $K^X\alpha L^N$ photon yields, neglecting the off-diagonal terms in Eq. (4). This way the initial values of η can be calculated without knowing the relative intensities $Y(K^X\alpha L^N)$ which depend on the collision parameters. Initial and final values of η obtained for Mg are shown in Fig. 2. As shown, only small deviations are observed between the initial and final values of the iterative procedure.

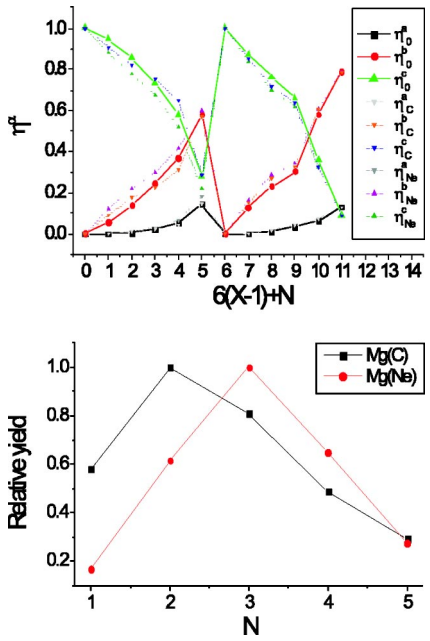

FIG. 2. Top: initial values of η (subscript 0) for the Mg metal target and the values obtained at the end of the iteration procedure for the C-induced spectrum (subscript C) and Ne-induced spectrum (subscript Ne). Bottom: the $K\alpha$ photon yield distributions for the two Mg spectra determined from $K\beta$ photon yields using decay schemes.

The accuracy of the calculated line shapes was not adequate to determine the values of η from the measured spectra. Since the spectra can be fitted using the calculated values, we estimate the errors of η corresponding to the largest contributions to be of the order of 10%. It should be stressed that the values of η which were used to determine the theoretical line shapes employed in the fit in order to help peak identification, do not have a significant effect on the intensities of the $K^X\alpha L^N$ lines.

For Mg and Si the $K\alpha$ hypersatellites cannot be resolved from the overlapping $K\beta$ satellites. A correct determination of the $K\alpha$ hypersatellite yields requires thus precise knowledge of the $K\beta$ satellite intensities. The latter can be determined from the resolved $K\alpha$ satellite yields with the help of decay schemes. First $K\alpha$ satellite yields are used in Eq. (4) to determine $I(K^X L^N)$. Since the same vacancy states give rise also to the $K\beta$ transitions, $Y(K^X\beta L^N)$ can be determined from Eq. (4), replacing $W_{rr}{}^\alpha$ with $W_{rr}{}^\beta$. Again the problem must be addressed iteratively.

Since $K\alpha$ satellites lie below, while $K\beta$ satellites lie above the K absorption edge, different absorption in the target must be accounted for. When the yield of at least one $K\beta$ satellite can be resolved in the measured spectra, the absorption edge effect can be excluded by fixing the $K\beta$ satellite yields according to that value (Fig. 2).

D. Spectra fitting

The model spectra S^T were built as a sum of line shapes:

$$S^T(E) = \sum_i Y_i T_i(E, E_i^C, w_i), \tag{7}$$

where T_i are the calculated line shapes discussed in Eq. (1) and Y_i the corresponding photon yields. The measured spectra consisted of $K\alpha$ satellites, $K\alpha$ hypersatellites, and $K\beta$ satellites up to fifth order. Since contributions of less than 5% to a specific satellite or hypersatellite were disregarded, the model contained about 30 components.

Relative intensities of components contributing to a specific $K\alpha$ satellite or hypersatellite were fixed to the values calculated in Sec. III C, so that only the $K\alpha$ satellite and hypersatellite yields $Y(K^X\alpha L^N)$ were varied. The $K\beta$ satellite yields were also fixed according to the values calculated in Sec. III C. In Mg spectra it was possible to determine lower-order $K\beta$ satellite yields directly from the measured spectra and fix the yields of higher-order $K\beta$ satellites which are overlapping the $K\alpha$ hypersatellites. Since in Si spectra none of the $K\beta$ satellite yields can be determined directly from the measured spectra, it was required that the $K\beta$ satellite yield ratios agree with the ones determined in Sec. III C.

The central energies E_i^C of the $K^X\alpha L^N c$ contributions can be resolved directly from the measured spectra. The central energies of other contributions were restricted by demanding that the values obtained in the carbon and neon induced spectra agree within 0.5 eV. This constraint is very helpful, since contributions corresponding to lower L-shell ionization are more pronounced in the carbon induced spectra, while those corresponding to higher order of L-shell ionization are more pronounced in the neon induced spectra.

For Mg, only the positions of the first three $K\beta$ satellites could be determined, while for Si at least one component of every $K\beta$ satellite was clearly resolved. Where the positions were uncertain, an equal energy spacing within a couple of eV between $K\beta$ satellites and also between the two components of each $K\beta$ satellites were required.

The values of w_i derived in Sec. III A. were used as a first guess and as the lower limit in the fitting procedure. The values obtained in the carbon- and neon-induced spectra were required to agree within 0.5 eV and to differ as little as possible from the estimated values.

The results of the fitting procedure for Mg and Si are presented in Figs. 3 and 4, respectively. Since peak identification below the K absorption edge is straightforward, only the carbon induced Mg spectrum is shown for this energy region.

IV. THEORETICAL CROSS SECTIONS

In the ion-atom collisions studied, direct Coulomb ionization and electron capture by the projectile are the major mechanisms responsible for atomic inner-shell ionization. The cross sections for multiple ionization of K, L, and M shells were calculated within the independent electron model, considering these two mechanisms and using single ionization probabilities obtained within the three-body classical trajectory Monte Carlo (CTMC) simulation [17]. The model used is described in detail in [18], while the initialization parameters are described in [19]. Single-electron direct and capture ionization probabilities obtained for 1*s*-, 2*s*-, and

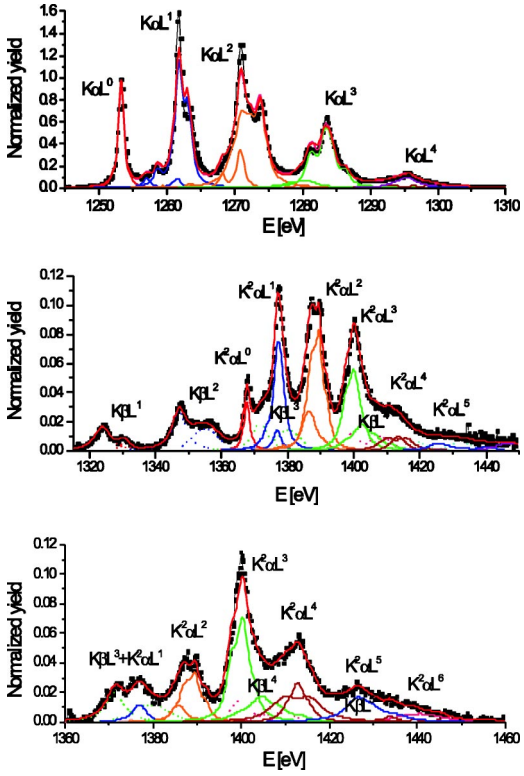

FIG. 3. Measured K x-ray spectra of Mg fitted with the model based on the calculated line shapes. The $K\alpha$ satellite and hypersatellite regions of the spectrum induced by C impact are shown in the upper and center graphs, respectively. The lower graph shows the $K\alpha$ hypersatellite region of the Ne induced spectrum. $K\alpha$ contributions are shown by solid lines and $K\beta$ by dotted lines.

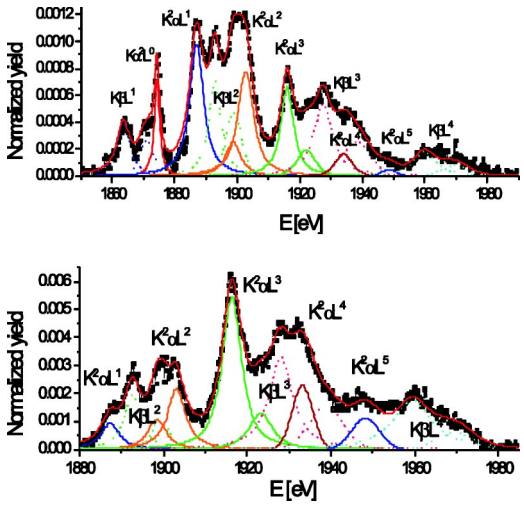

FIG. 4. Measured and modeled $K\alpha$ hypersatellite spectra of Si induced by C (top) and Ne (bottom) impact. The spectra were modeled with pseudo-Voigt curves, using several curves when such a need was observed in the Mg spectra. $K\alpha$ contributions are shown by solid lines and $K\beta$ by dotted lines.

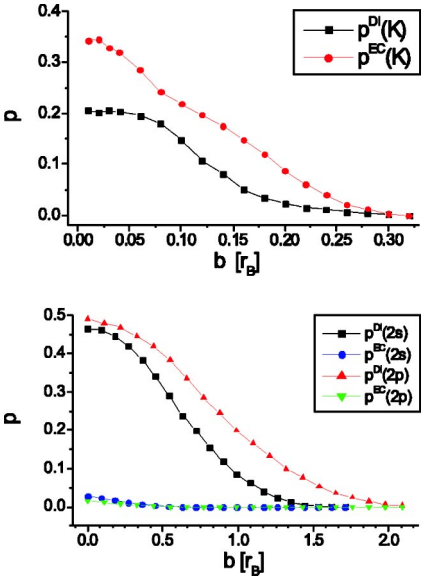

FIG. 5. CTMC direct ionization (DI) and electron capture (EC) single-electron probabilities calculated for *K*- (top) and *L*- (bottom) shell electrons of Mg atoms in collisions with 34-MeV C ions as a function of impact parameter. The corresponding *K*- and *L*-shell radii of Mg are $0.13r_B$ and $0.69r_B$, respectively. For each point plotted in the figure, 20 000 trajectories were calculated.

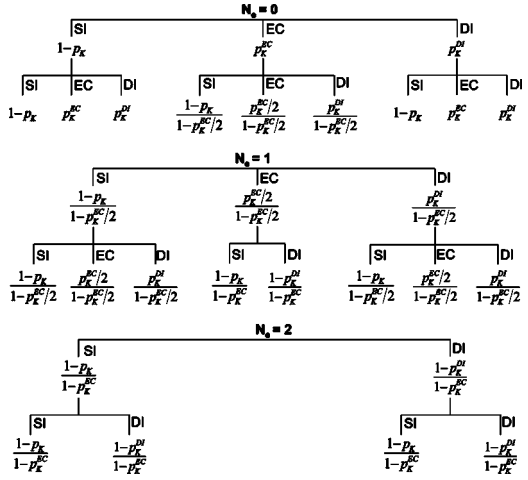

FIG. 6. Schematic view of the two-step double-*K*-shell ionization resulting from direct ionization (DI) and electron capture (EC) into the projectile's *K* shell. (SI) denotes elastic scattering. The single-electron probabilities indicated in the scheme are the CTMC predictions calculated for bare projectiles. The two-step model is needed, since electron capture probabilities are inversely proportional to the number of electrons (N_e) in the projectile's *K* shell. We must separate the case of a bare projectile ($N_e=0$), projectile with one-*K*-shell electron ($N_e=1$), and projectile with *K* shell full ($N_e=2$), where only direct ionization contributes to the double-*K*-shell ionization.

$2p$-subshell electrons of Mg bombarded with 34-MeV C ions are shown in Fig. 5.

The calculations showed that for the collisions studied, *L*- and *M*-shell ionization is dominated completely by the direct ionization. Since electron capture into the projectile's *K* shell is approximately 10 times larger than capture into outer shells, only the *K*-*K* transfer channel was considered. In this case there is no coupling between the ionization of different shells, and the cross sections in the independent electron approximation can be written as

$$\sigma(K^X L^N) = \int 2\pi P(M^H)(b) P(L^N)(b) P(K^X, N_e)(b) b db, \tag{8}$$

where $P(K^X,N_e)$, $P(L^N)$, and $P(M^H)$ are the probabilities for the multiple ionization in the *K*, *L*, and *M* shells, respectively, and *b* is the impact parameter. By N_e we have explicitly denoted the dependence of the *K*-shell ionization on the number of electrons in the projectile's *K* shell.

When direct ionization is the only important mechanism, the ionization probabilities can be approximated by the binomial expression

$$P(X^N)(b) = \binom{X_0}{N} p_X^{DI}(b)^N (1 - p_X^{DI}(b))^{8-N}, \tag{9}$$

where p_X^{DI} is the single-electron direct ionization probability of the *X* shell, *N* is the number of vacancies produced, and X_0 is the number of electrons in the shell before collision.

Electron capture is possible only when there is a vacancy in the projectile's *K* shell. Since this limitation stems from quantum mechanics, it is not incorporated in CTMC simulations. The CTMC capture probabilities are valid only for fully stripped projectiles ($N_e=0$). For not completely stripped projectiles, however, single-electron capture probabilities can be assumed to be proportional to the number of electrons in the projectile's *K* shell. This dependence of the capture cross section on the projectile's charge has already been confirmed [6–8].

When considering double-*K*-shell ionization, a change in the ionization probabilities after electron capture in the projectile *K* shell must be considered. *K*-shell ionization was thus treated as a two-step process, shown in Fig. 6. The probabilities $P(K,N_e)$ are determined from the scheme by multiplying the terms for the first and second electrons and summing the terms leading to the desired state.

Since projectiles in solid media acquire different charge states, the ionization cross section measured with solid targets must be written as

$$\sigma(K^X) = \sum P_e(N_e)\sigma(K^X, N_e), \tag{10}$$

where $P_e(N_e)$ represents the probability for a certain projectile charge state in solid media. The projectile's charge-state distributions depend on the projectile's energy and atomic number and were obtained from [20,21]. In Table I the calculated double- to single-*K*-shell ionization ratios for all possible projectile charge states can be found.

V. RESULTS

Using the fitting procedure described in Sec. III D, $K\alpha$ satellite and hypersatellite photon yields Y_r^α were extracted

TABLE I. Experimental (Expt.) and theoretical double- to single-*K*-shell ionization cross-section ratios for the measured collisions. The ratios and relative errors (in parentheses) are given in %. The theoretical ratios were calculated for projectiles with zero, one- and two-*K*-shell electrons (*0*, *1*, *2*), and for projectiles with equilibrium charge-state distribution in the target (*av*).

	$\sigma_d/\sigma_s(0)$	$\sigma_d/\sigma_s(1)$	$\sigma_d/\sigma_s(2)$	$\sigma_d/\sigma_s(av)$	Expt.
Mg+34 MeV C	16.6	12.3	10.2	15.8	33 (30)
Mg+50 MeV Ne	24.1	12.5	11.7	15.3	12 (25)
Si+34 MeV C	12.2	8.4	7.6	11.6	9.6 (20)
Si+50 MeV Ne	12.2	7.5	8.2	9.0	9.0 (25)

for the four investigated collisions. Photon yields are related to the vacancy-state production yields by Eq. (4), which are proportional to ionization cross sections. Since the matrix in Eq. (4) is upper diagonal, the normalized $\sigma(K^2L^5)$ ionization cross sections were determined first, then $\sigma(K^2L^4)$, and all the way to $\sigma(K^1L^0)$.

After ionization cross sections are determined, relative contributions from different K^XL^N states to a specific $K^X\alpha L^N$ photon yield can be obtained. As shown in Fig. 7, several initial states contribute to a particular $K^X\alpha L^N$ photon yield. The effect is more pronounced in the case of Mg, due to the metallic character of solid Mg, where the number of *M*-shell electrons is not reduced during the decay scheme, making the schemes significantly larger. Since the contribution to $K\alpha$ satellite yields of initial states with two *K*-shell vacancies increases with the satellite order, there is a shift in the $K\alpha$ satellite photon yield distributions to higher order as compared to the distributions of the initial-state production yields.

The distributions of the KL^N and the K^2L^N initial-state production yields are shown in Fig. 8. Within the independent electron model, the distributions should not depend on the number of vacancies in the *K* shell. The distributions shown in Fig. 8 agree with this statement within the experimental error, but a systematic shift of the distributions corresponding to the K^2L^N states towards higher orders of *L*-shell ionization can be seen. The shift which was observed for the four investigated collisions might indicate that the yields of higer-order $K\beta$ satellites, which are overlapping the $K\alpha$ hypersatellites were underestimated in our analysis. In the Mg spectra the $K\beta L^4$ and $K\beta L^5$ satellites are completely hidden by the stronger $K\alpha$ hypersatellites and their yields are practically undetermined in the measured spectra. By adjusting these two $K\beta$ satellite yields so that the KL^N and K^2L^N initial-state production yield distributions would match, an approximately 25% decrease in the overall double-*K*-shell vacancy production yield was obtained. $K\beta$ satellite yields are better determined in the case of Si. Here $K\beta L^2$ and $K\beta L^3$ photon yields were adjusted. The increase of $K\beta$ satellite yields needed to match the KL^N and the K^2L^N vacancy yield distributions was the same within the errors for all four spectra, supporting our assumption that the calculated yields of higher-order $K\beta$ satellites were underestimated.

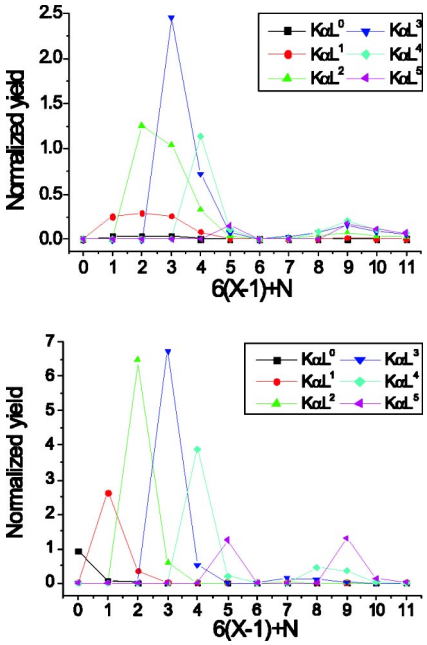

FIG. 7. Contributions of different K^XL^N states to the $K\alpha L^N$ photon yields in the Ne-Mg collisions (top) and Ne-Si collisions (bottom).

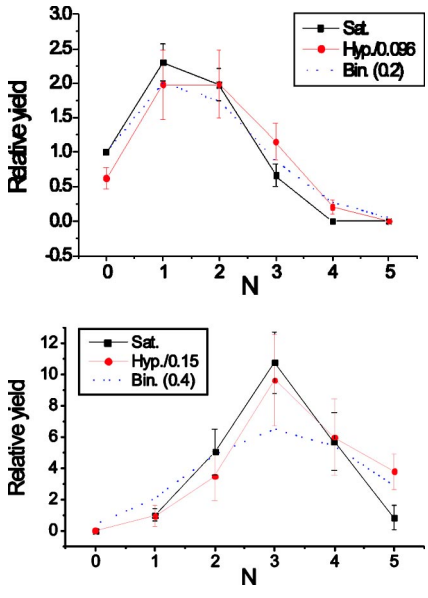

FIG. 8. Initial vacancy production yield distributions for states with one (Sat) and two holes (Hyp) in the *K* shell for C-Si collisions (top) and Ne-Mg collisions (bottom). The dotted lines correspond to the best fits to the binomial distribution.

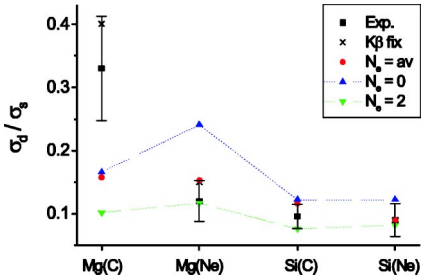

FIG. 9. Comparison of the experimental double- to single-*K*-shell ionization ratios σ_d/σ_s obtained in the present work with theoretical predictions computed in Sec. IV. Since the theoretical values depend on the projectile's charge, the values calculated for bare projectiles ($N_e=0$), projectiles with two 1*s* electrons ($N_e=2$), and projectiles with the equilibrium charge in solid media ($N_e=av$) were plotted. For Mg the ratios obtained by fixing the $K\beta L^4$ and $K\beta L^5$ intensities to the calculated values are also presented ($K\beta$ fix).

For each collision, the KL^N and the K^2L^N initial-state production yields were fitted with a binomial distribution, as expected from the independent electron model. From the independent electron model values of 0.47, 0.75, 0.43, and 0.70 in the case of C-Mg, Ne-Mg, C-Si, and Ne-Si collisions are expected for $p_L(0)$, while from the fit values 0.25, 0.4, 0.2, and 0.3 with an error of 0.05 were obtained. The values $p_L(0)$ represent the *L*-shell ionization probabilities for near-central collisions [22] and were found to be approximately twofold smaller than expected from the CTMC calculations. Deviation of distributions from the binomial shape was also observed.

The double- to single-*K*-shell ionization cross-section ratios were determined as

$$\frac{\sigma_d}{\sigma_s}=\frac{\sum_{N=0}^{5}\sigma(K^2L^N)}{\sum_{N=0}^{5}\sigma(KL^N)}=\frac{\sum_{N=0}^{5}I(K^2L^N)}{\sum_{N=0}^{5}I(KL^N)}. \qquad (11)$$

Results are presented in Table I. Quoted errors originate from experimental error, uncertainties in the *W* matrix (estimated to 5%–10%), and the uncertainties of the $K\beta$ satellite yields overlapping the $K\alpha$ hypersatellite part (approximately 15%). In Fig. 9 the experimental ratios for the double- to single-*K*-shell ionization cross sections are compared with the theoretical predictions presented in Sec. IV. A satisfactory agreement is observed except for the C-Mg collision for which the experimental value is twofold bigger than the theoretical one. We are inclined to believe that this discrepancy may have an experimental origin. The setup of the C beam was indeed slightly changed during the measurement, which could have affected the normalization of the hypersatellite part of the spectrum with respect to the satellite part.

VI. SUMMARY AND CONCLUSION

Mg and Si solid targets were bombarded by 34-MeV C and 50-MeV Ne ions, and the *K* x-ray emission was recorded using a wavelength dispersive crystal spectrometer. The instrumental energy resolution of about 0.5 eV enabled us to resolve $2p\rightarrow 1s$ radiative transitions of singly and doubly *K*-shell-ionized atoms with up to five additional *L*-shell vacancies.

In light elements such as Mg and Si, spectral contributions $K^X\alpha L^N$ cannot be approximated by single peaks. The line shapes of spectral contributions were calculated by the GRASP92 computer code. In the case of Mg, the calculated $K\alpha$ line shapes obtained by calculating the energies of initial and final states separately and considering configuration mixing with configurations obtained from the original ones by substitutions $3s^2\rightarrow 3p^2$ and $2s^2\leftrightarrow 2p^2$ were found to reproduce the measured shapes within a precision of 0.2 eV. These theoretical shapes were used to model the measured spectra. As for Si a poor agreement was observed between the theoretically determined line shapes and the experimental ones; the Si spectra were modeled using pseudo-Voigt curves. The number of pseudo-Voigt curves used to model a specific contribution was determined from the theoretical line shape of the corresponding contribution in the Mg spectrum.

In order to determine the initial-state production yields from the corresponding photon yields, decay schemes of multiply ionized Mg and Si atoms were calculated and the relation was given in a matrix formulation. From the decay schemes the relative photon yields of components contributing to a specific $K\alpha$ satellite or hypersatellite were determined, and the $K\beta$ satellite yields from $K\alpha$ satellite yields were deduced. The so-obtained values were incorporated in the model to make it well determined and credible. The calculated relative photon yields of components contributing to a specific $K\alpha$ satellite or hypersatellite were found to be a good estimate, while the yields of higher-order $K\beta$ satellites were underestimated by our calculations.

From the initial-state production yields, *L*-shell ionization probabilities and double- to single-*K*-shell ionization cross-section ratios were determined. The corresponding theoretical values were calculated within the independent electron approximation using single-electron probabilities from the CTMC model. While the calculated *L*-shell probabilities overestimated the experimental ones by approximately a factor of 2, an agreement between the experimental and theoretical values for double- to single-*K*-shell ionization cross sections was found. An exception was the C-Mg collision, in which experimental problems were most probably encountered.

We have demonstrated that, for nearly symmetric collisions of heavy ions with light elements such as Mg and Si, the spectra are very complex. Due to the energy overlap of $K\beta$ satellites and $K\alpha$ hypersatellites, high-resolution spectrometry employing crystal spectrometers is essential for proper peak identification. Even so, careful modeling of the spectra, based on detailed theoretical calculations, is further required to properly identify separate contributions. It was also shown that there are significant differences between the initial-state production yield distributions and the photon yield distributions.

ACKNOWLEDGMENTS

The authors thank Dr. Schmelzbach and the PSI Philips cyclotron crew for providing good beam conditions, M. Ber-

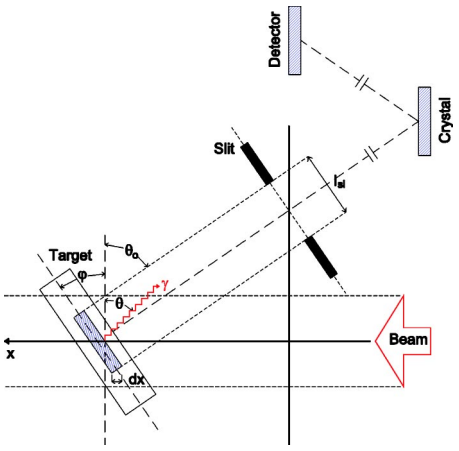

FIG. 10. Schematic view of the beam-target geometry used in the present experiment.

set for his help during the measurements, and M. Žitnik for theoretical consultations. This work was supported by the Slovenian Ministry of Education, Science and Sport of Slovenia through the research program "Low Energy Physics" (Grant No. PO-0521-0106-02), by the Swiss National Science Foundation, and through a bilateral Scientific and Technological Cooperation between Slovenia and Hungary (Project No. BI-HU/04-05-013).

APPENDIX

In this appendix the procedure leading to Eq. (5) that incorporates a self-absorption factor accounting for the stopping of the projectile in the target and absorption of photons on their way out will be outlined. Since the photon absorption and projectile energy depend on the penetration depth, the target was sliced into thin layers in which the projectile energy and the photon absorption can be considered constant. The beam-target geometry of our experiment is presented schematically in Fig. 10. The slit width l_{sl} was small enough that the emission angle θ and central angle θ_0 could be assumed equal. The photon yield from the target layer at depth x can be determined from Eq. (4):

$$dY_i \propto \sum_j W_{rr}(i,j)\sigma_j(E_0)s_j(E)\exp\left(-\frac{\mu_i \cos(\varphi)}{\sin(\theta_0+\varphi)}x\right)dV. \tag{A1}$$

Indices i,j correspond to a particular $K^X L^N$ state through $i,j=6(X-1)+N+1$. The angles are depicted in Fig. 10, while dV represents the volume of the slice. In Eq. (A1) the ionization cross section was written as a product $\sigma(E_0)s_j(E)$ in order to separate the absolute value at the impact energy from its energy dependence, which can be more accurately predicted by theory. The energy dependence was calculated with the model presented in Sec. IV. The exponential term in Eq. (A1) describes the absorption of the photons in the target. The absorption coefficients μ were taken from the tables of Thinh and Leroux [23]. The energy of the projectile at a depth x was calculated from

$$E(x+dx) = E(x) + S(E)dx, \tag{A2}$$

where the stopping powers $S(E)$ were taken from Ziegler and Manoyan [24]. Using Eq. (A2), the contributions from thin layers given in Eq. (A1) can be summed over the target thickness d:

$$Y_i \propto \sum_j W_{rr}(i,j)\left[\sum_{x=0}^{d/\cos\varphi} s_j(E(x)) \times \exp\left(-\frac{\mu_i \cos(\varphi)}{\sin(\theta_0+\varphi)}x\right)dV\right]\sigma_j(E_0). \tag{A3}$$

The term in the squared brackets can be written as a matrix, yielding the final equation

$$Y_i \propto \sum_{j\geq i} W_{rr}(i,j)F_T(i,j)\sigma_j(E_0), \tag{A4}$$

which has been used in Sec. IV.

When thin foils are used, the energy loss of the projectiles in the target can be neglected and $s_j(x)=1$ for all j. In such cases all the elements in the ith row of the F_T can be written simply as

$$F_T(i) \propto \frac{1}{\mu_i}\left[1-\exp\left(-\frac{\mu_i}{\sin(\theta_0+\varphi)}d\right)\right]. \tag{A5}$$

[1] P. Richard, W. Hodge, and C. F. Moore, Phys. Rev. Lett. **29**, 393 (1972).
[2] D. Olsen and C. F. Moore, Phys. Rev. Lett. **33**, 194 (1974).
[3] P. Richard, D. K. Olsen, R. Kauffman, and C. F. Moore, Phys. Rev. A **7**, 1437 (1973).
[4] V. Cindro, M. Budnar, M. Kregar, V. Ramšak, and Ž. Šmit, J. Phys. B **22**, 2161 (1989).
[5] B. Boschung, J.-Cl. Dousse, B. Galley, Ch. Herren, J. Hoszowska, J. Kern, Ch. Rhême, Z. Halabuka, T. Ludziejewski, P. Rymuza, Z. Sujkowski, and M. Polasik, Phys. Rev. A **51**, 3650 (1995).
[6] J. Hall, P. Richard, T. J. Gray, and C. D. Lin, Phys. Rev. A **24**, 2416 (1981).
[7] J. Hall, P. Richard, P. L. Pepmiller, D. C. Gregory, P. D. Miller, C. D. Moak, C. M. Jones, G. D. Alton, L. B. Bridwell, and C. J. Scofield, Phys. Rev. A **33**, 914 (1986).
[8] L. C. Tribedi, K. G. Prasad, P. N. Tandon, Z. Chen, and C. D. Lin, Phys. Rev. A **49**, 1015 (1994).
[9] J. Hoszowska, J.-Cl. Dousse, J. Kern, and Ch. Rhême, Nucl. Instrum. Methods Phys. Res. A **376**, 129 (1996).
[10] R. W. James, *The Optical Principles of Diffraction of X-rays* (Bell, London, 1950).
[11] J. L. Campbell and T. Papp, At. Data Nucl. Data Tables **77**, 1 (2001).

[12] J. P. Mossé, P. Chevallier, and J.-P. Briand, Z. Phys. A **322**, 207 (1985).
[13] F. P. Larkins, J. Phys. B **4**, L29 (1971).
[14] S. T. Perkins, D. E. Cullen, M. H. Chen, J. H. Hubbell, J. Rathkopf, and J. Scofield (unpublished).
[15] I. P. Grant, B. J. McKenzie, P. H. Norrington, D. F. Mayers, and N. C. Pyper, Comput. Phys. Commun. **21**, 207 (1980).
[16] T. W. Tunnel and C. P. Bhalla, Phys. Lett. **86A**, 13 (1981).
[17] E. W. McDaniel, J. B. A. Mitchell, and M. E. Rudd, *Atomic Collisions: Heavy Particle Projectiles* (Wiley, New York, 1993).
[18] K. Tökési and A. Kövér, J. Phys. B **33**, 3067 (2000).
[19] C. O. Reinhold and C. A. Falcón, Phys. Rev. A **33**, 3859 (1986).
[20] K. Shima, T. Mikumo, and H. Tawara, At. Data Nucl. Data Tables **34**, 357 (1986).
[21] H. D. Betz, Rev. Mod. Phys. **44**, 465 (1972).
[22] J. M. Hansteen and O. P. Mosebekk, Phys. Rev. Lett. **29**, 1361 1972).
[23] T. P. Thinh and J. Leroux, X-Ray Spectrom. **8**, 85 (1979).
[24] J. F. Ziegler and J. Manoyan, Nucl. Instrum. Methods Phys. Res. B **35**, 215 (1988).